BIOPHYSICS

Actuating tension-loaded DNA clamps drives membrane tubulation

Longfei Liu[1,2], Qiancheng Xiong[1,2], Chun Xie[1,2], Frederic Pincet[1,2,3], Chenxiang Lin[1,2,4]*

Membrane dynamics in living organisms can arise from proteins adhering to, assembling on, and exerting force on cell membranes. Programmable synthetic materials, such as self-assembled DNA nanostructures, offer the capability to drive membrane-remodeling events that resemble protein-mediated dynamics but with user-defined outcomes. An illustrative example is the tubular deformation of liposomes by DNA nanostructures with purposely designed shapes, surface modifications, and self-assembling properties. However, stimulus-responsive membrane tubulation mediated by DNA reconfiguration remains challenging. Here, we present the triggered formation of membrane tubes in response to specific DNA signals that actuate membrane-bound DNA clamps from an open state to various predefined closed states, releasing prestored energy to activate membrane deformation. We show that the timing and efficiency of vesicle tubulation, as well as the membrane tube widths, are modulated by the conformational change of DNA clamps, marking a solid step toward spatiotemporal control of membrane dynamics in an artificial system.

INTRODUCTION

Many cellular processes, such as cell division, vesicular transport, and virus infection, involve the tubular deformation of lipid bilayer membranes (*1*). Typically, membrane tubulation results from membrane-interacting proteins convening at specific locations in certain orders (*2*–*4*). The well-orchestrated process is coordinated by chemical or mechanical signals responsible for protein recruitment, assembly, disassembly, and conformational change. To better understand the working principle of the cells' arsenal of membrane-deforming machines, a useful practice is to build artificial nanodevices that perform similar tasks on model membranes. Toward this goal, scientists have built a variety of DNA nanostructures that bind lipid bilayers via membrane anchors (e.g., cholesterol and amphipathic peptides) (*5*–*8*). A subset of these nanostructures, designed to mimic BAR domains, dynamin, or the endosomal sorting complex required for transport (ESCRT), can draw membrane tubes from vesicles and supported bilayers (*9*–*11*). The programmable geometry and membrane anchor placement of the DNA nanostructures provide control over parameters that are not readily tunable when working with naturally existing proteins (e.g., membrane affinity, stiffness, and self-assembling pattern), thereby shedding light on the determinants of membrane tubulation. However, early examples of membrane-tubulating DNA structures work autonomously, that is, without an on switch to the remodeling process after covering membranes with DNA (*9*, *12*, *13*). Although linker strand and Mg^{2+}-mediated DNA origami polymerization have been shown to induce membrane bulging or tubulation, the membrane-remodeling outcomes, particularly the morphology of the deformed membranes, do not necessarily conform to the designed shape of the membrane-coating DNA structures (*10*, *11*, *14*, *15*). Moreover, existing membrane-sculpting DNA structures are designed to adopt a single stable conformation, thus lacking the ability to process biochemical signals via conformational changes, a mechanism used by proteins such as ESCRT-III and dynamin to generate and constrict membrane tubes.

To engineer trigger-responsive DNA devices for better spatiotemporal control of membrane tubulation, we tapped into dynamic DNA nanotechnology, which has developed molecular machines with movable parts and controllable nanoscale motions (*16*–*20*). We are especially interested in a class of mechanical DNA devices, where the bending of a multi–DNA helix beam can be actuated by the cleavage, folding, or unfolding of single-stranded DNA (ssDNA) domains (*21*–*23*). On the basis of the hypothesis that bending membrane-anchored DNA nanostructures—specifically their membrane-binding interface—would elicit corresponding curvature changes of lipid bilayers, we built cholesterol-modified DNA clamps containing a prestressed DNA bridge held open by a group of tension-loaded ssDNA strings. Releasing tension via toehold-mediated strand displacement triggered the DNA clamps to close and, in turn, led to tubular deformation of liposomes covered by DNA clamps. These DNA clamps thus allowed for on-demand membrane tubulation triggered by specific signals. Closing DNA clamps after membrane binding resulted in substantially higher tubulation efficiency than deploying preclosed DNA clamps to the membrane, possibly because of better membrane-anchor accessibility in the open clamps and simultaneous energy dissipation during the DNA structure actuation. We showed that DNA clamps with different closed states deformed giant unilamellar vesicles (GUVs) into tubes with different width, highlighting the programmability of these membrane-sculpting devices.

RESULTS

DNA clamp design and assembly

We designed a tension-loaded DNA clamp consisting of two 12–helix bundle piers (each 14 nm long) joined by a 4–helix bundle bridge (14 nm long) and four ssDNA strings (Fig. 1A, left) (*24*). The geometry of an open clamp is codetermined by the gradient of base pair (bp) insertion/deletion (indel) installed in its bridge, which dictates the structure's curvature at the tension-free state (i.e., closed state) (*25*), and the lengths of the tensioned strings, which counteract the

[1]Department of Cell Biology, Yale University School of Medicine, New Haven, CT, USA. [2]Nanobiology Institute, Yale University, West Haven, CT, USA. [3]Laboratoire de Physique de l'Ecole Normale Supérieure, Ecole Normale Supérieure (ENS), Université Paris Sciences et Lettres (PSL), CNRS, Sorbonne Université, Université Paris Cité, Paris, France. [4]Department of Biomedical Engineering, Yale University, New Haven, CT, USA.
*Corresponding author. Email: chenxiang.lin@yale.edu

effect of the indels and hold the clamp open (*26*, *27*). For example, a bridge with a ±5-bp indel pattern held by four ~44-nucleotide (nt) strings should theoretically bend slightly (~18°) in the open clamp and, upon releasing the tensioned (each ~10 pN) strings, close to a higher bending angle of ~63° (figs. S1 and S2 and table S1; also see the "Prediction of the bending angle of clamps" section in the Supplementary Materials for details) (*25*, *26*, *28*). To facilitate the tension release, we added an 8-nt-long overhang to the 5′ end of each ssDNA string, which serves as a toehold to initiate strand displacement when exposed to DNA triggers to detach one end of the strings from the pier (Fig. 1A, right). The DNA clamp thus stores energy ready to be released by specific DNA triggers in the form of mechanical deformation. Unlike the existing DNA devices that bend in the same direction as the signal-sensing ssDNA domains (*22*, *23*), we purposely placed ssDNA strings on the opposite side of the concave surface, so that the DNA triggers have unfettered access to the strings of the membrane-bound clamp.

We first prepared the open DNA clamps following a well-established DNA origami folding and purification pipeline. Briefly, annealing the mixture of a 1512-nt-long circular ssDNA (scaffold strand) and a pool of staple strands led to the self-assembly of open clamps, albeit as a minor product (fig. S3). To deter the formation of unwanted dimeric structures, we omitted two staple strands in the bridge in the initial annealing and added them back to the folding mixture for a second round of annealing (*29*), which helped the correctly folded open clamps become the dominant product (fig. S4 and see Materials and Methods for details). Adding DNA triggers to the purified open clamps (trigger:clamp = 40:1, mol/mol) turned them into the closed conformation within 1 hour at room temperature, as shown in the negative-stain transmission electron microscopy (TEM) images (Fig. 1A).

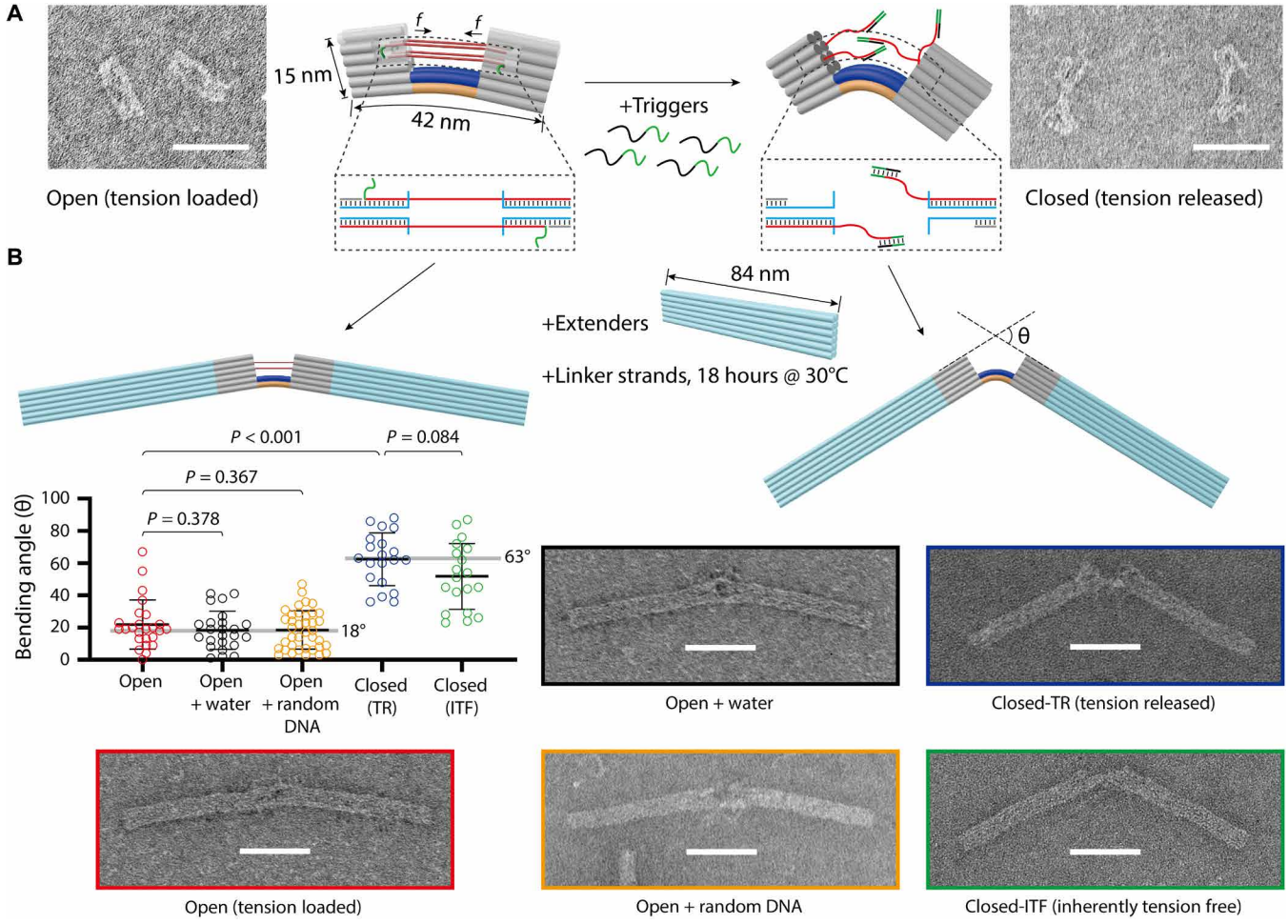

Fig. 1. Actuating DNA clamps by triggered strand displacement. (**A**) Left: An open, tension-loaded clamp consisted of two straight piers (gray cylinders), joined by one bridge (blue/orange cylinders at the bottom) and four ssDNA strings (red lines with green toehold at the top). The near-flat shape results from the balance between the curved bridge and the tensioned strings. Right: Upon toehold-mediated strand displacement (trigger strands shown as black curls with green toeholds), one end of the strings is detached from the pier, resulting in a closed, tension-released clamp with increased bending. Insets contain strand diagrams showing the two front strings before and after strand displacement. Negative-stain TEM images are shown next to the schematics. Scale bars, 50 nm. This experiment was repeated three times (technical replicates) with similar results. (**B**) Top: Schematics of attaching DNA extenders (cyan, used for measuring angles only) to both ends of the clamp with the help of a set of linker strands. Bottom: Bending angle distributions (showing all data points with means ± SD) of DNA clamps in various states and representative TEM images of extender-attached DNA clamps. Adding water or DNA with random sequences to open clamps serves as negative controls. Predicted bending angles of the open and closed clamps (18° and 63°, respectively) are noted in the plot for reference. *P* values are produced by unpaired two-tailed Student's *t* test (two-group comparison). TR, tension released; ITF, inherently tension free. Scale bars, 50 nm.

To allow for better visualization of the DNA clamp structure and reconfiguration, we built two 84-nm-long DNA extenders to attach to both ends of the clamp (Fig. 1B) via linker strands designed to bridge unpaired scaffold-strand loops at the ends of the DNA origami structures (figs. S5 and S6). As expected, the TEM images of the clamps became much easier to analyze after extender attachment. We measured the bending angles of the open, tension-loaded clamps and closed, tension-released clamps to be 22° ± 15° (N = 25) and 62° ± 16° (N = 20), respectively, in good agreement with theoretical values. In contrast, adding water or DNA strands with random sequences (i.e., without sequence complementarity to the ssDNA strings) to the open clamps did not significantly change their bending angle (18° ± 12°, N = 24 and 19° ± 12°, N = 38, respectively), confirming that the DNA trigger–mediated strand displacement caused the structural transformation. In addition, we folded clamps without the ssDNA strings (i.e., in an inherently tension-free state; figs. S1 and S3), purified them, and measured their bending angle to be 52° ± 20° (N = 19). We note that the DNA clamps after open-to-close reconfiguration are practically indistinguishable from the inherently tension-free clamps in their bending angle distributions, supporting an efficient structural transformation via the tension-release mechanism. Note that the extenders were built for angle determination only and were not added to the DNA clamps in subsequent membrane tubulation experiments.

Actuating membrane-bound DNA clamps tubulates vesicles

The stimuli-responsive, flat-to-curved reconfiguration of DNA clamps remotely mimics the conformational change of dynamin, a guanosine triphosphatase responsible for membrane tubule constriction during endocytosis (*4*). To enable membrane binding of the DNA clamps, we extended eight ssDNA handles from the concave surface of the clamp for proximal attachment of cholesterol moieties (spaced evenly at ~5.4 nm) as membrane anchors (depicted as green ellipsoids in Fig. 2A). In addition, we labeled the clamp with four copies of Alexa Fluor 647 (depicted as red stars in Fig. 2A) to facilitate fluorescence microscopy characterization. Figure 2A illustrates the experimental procedures for testing the DNA clamp's membrane-binding and membrane-deforming activities. Briefly, cholesterol-modified, tension-loaded clamps were mixed with lipid vesicles [99.2 mole percent (mol %) of 1,2-dioleoyl-*sn*-glycero-3-phosphocholine (DOPC) and 0.8 mol % of 1,2-dioleoyl-*sn*-glycero-3-phosphoethanolamine-*N*-(lissamine rhodamine B sulfonyl) (Rhod-PE)] at a clamp-to-lipid molar ratio of 1:1000, which translates to a theoretical 100% membrane coverage; the mixture was incubated for 1 hour to allow for binding. Subsequently, trigger strands were added; the strand displacement reaction was allowed to run for 1 hour. The entire procedure was carried out at room temperature while keeping osmolarity nearly constant. The only source of osmolarity change came from the addition of trigger strands (dissolved in water), which put the GUVs in a mild (~3% change in osmolarity) hypotonic solution. This is different from previous work that leveraged hyperosmotic conditions to promote DNA-mediated membrane deformation (*9*, *30*, *31*).

To examine the effect of DNA reconfiguration on membrane morphology, we started with large unilamellar vesicles (LUVs) prepared by lipid-film rehydration and extrusion. After coincubation with cholesterol-modified DNA clamps in the open conformation, LUVs showed a dense coat of DNA structures under TEM (Fig. 2B). Most LUVs retained their spherical shape, with only ~2% appearing to be deformed at this stage. To further evaluate the membrane binding of DNA clamps, the mixture of DNA clamps and LUVs was loaded to the bottom of an iodixanol gradient and spun at 48,000 rpm for 5 hours. Fluorescence scanning and gel electrophoresing the fractions recovered from a postcentrifugation gradient showed that virtually all vesicles comigrated with DNA to the upper half of the gradient, indicating considerably strong binding between the two, while unbound DNA remained at the bottom (fig. S7). We observed a surge of tubular structures (diameter: 36.5 ± 9.2 nm; table S2) after treating LUVs covered by open clamps with trigger strands, suggesting that membrane tubulation occurred as the result of the conformational change of DNA clamps. Among the deformed vesicles (~12% of all LUVs), some retained a spherical body with outward protrusions, while others turned entirely into a tube. All membrane tubes were covered by DNA structures (Fig. 2B). To study the influence of the membrane coverage by DNA clamps on vesicle tubulation efficiency, we varied the DNA clamp concentration to achieve a theoretical membrane coverage of 0, 50, 100, and 125%. Upon releasing the tension of the DNA clamps, the vesicle tubulation efficiency, defined as the portion of vesicles displaying tubular structures among all vesicles >100 nm in diameter, positively correlated with the initial DNA clamp concentration (fig. S8). Tubulation was not detected on vesicles free of DNA clamps. At 50% surface coverage, membrane tubes formed on only 3.0% of LUVs (N = 201). Increasing the coverage to 100% enhanced tubulation efficiency nearly fourfold, reaching 11.9% (N = 67). Further increasing the DNA clamp concentration resulted in a modest increase in DNA tube abundance (efficiency = 17.7% at 125% coverage, N = 333). These results are consistent with the concentration-dependent membrane-remodeling effects of DNA structures, further supporting the role of the structure-switching DNA clamp in driving vesicle tubulation (*9*, *10*).

To capture the DNA-mediated membrane dynamics in real-time, we next used GUVs (prepared by electroformation) as model membranes. After a 1-hour coincubation of open DNA clamps (~20 nM) with preadsorbed GUVs on a glass slide, trigger strands were introduced to initiate the strand displacement (defined as time 0). The DNA clamp concentration is comparable to those of the ESCRT-mimicking nanosprings (4 to 20 nM) (*10*) and the BAR-mimicking DNA structures (1 to 2 nM) (*9*) that tubulate GUVs, considering that a DNA clamp has only $^1/_3$ to $^1/_{10}$ of the membrane-binding area of those previously reported structures. We monitored the membrane tubulation on GUV membranes using confocal fluorescence microscopy for 1 hour (Fig. 2C, left, and movies S1 and S2). In two time-course studies, outward membrane tubulation became visible at ~10 min. In the next 10 to 30 min, tubules grew in length and quantity. Continued incubation for up to 1 hour led to further extension of membrane tubules and distortion of the GUV body. Furthermore, the tubular structures showed both rhodamine (from lipid) and Alexa Fluor 647 (from DNA) fluorescence, suggesting that the membrane tubes were wrapped by DNA clamps, which was corroborated by TEM imaging of tubulated GUVs (Fig. 2C, right). These tubes were wider (diameter = 62.1 ± 10.3 nm) than those originating from LUVs, presumably because of a larger lipid reservoir and the lower membrane tension of GUV. After 1 hour of strand displacement, ~61.5% GUVs (N = 39) showed at least one tubular protrusion on the surface (Fig. 3, A and D). As expected, we did not detect any tubular deformation on GUVs covered with open clamps, before (N = 38) or after the addition of water (N = 39) or DNA with random sequences (N = 25) in place of the DNA triggers. Unexpectedly, when GUVs were incubated with inherently tension-free clamps,

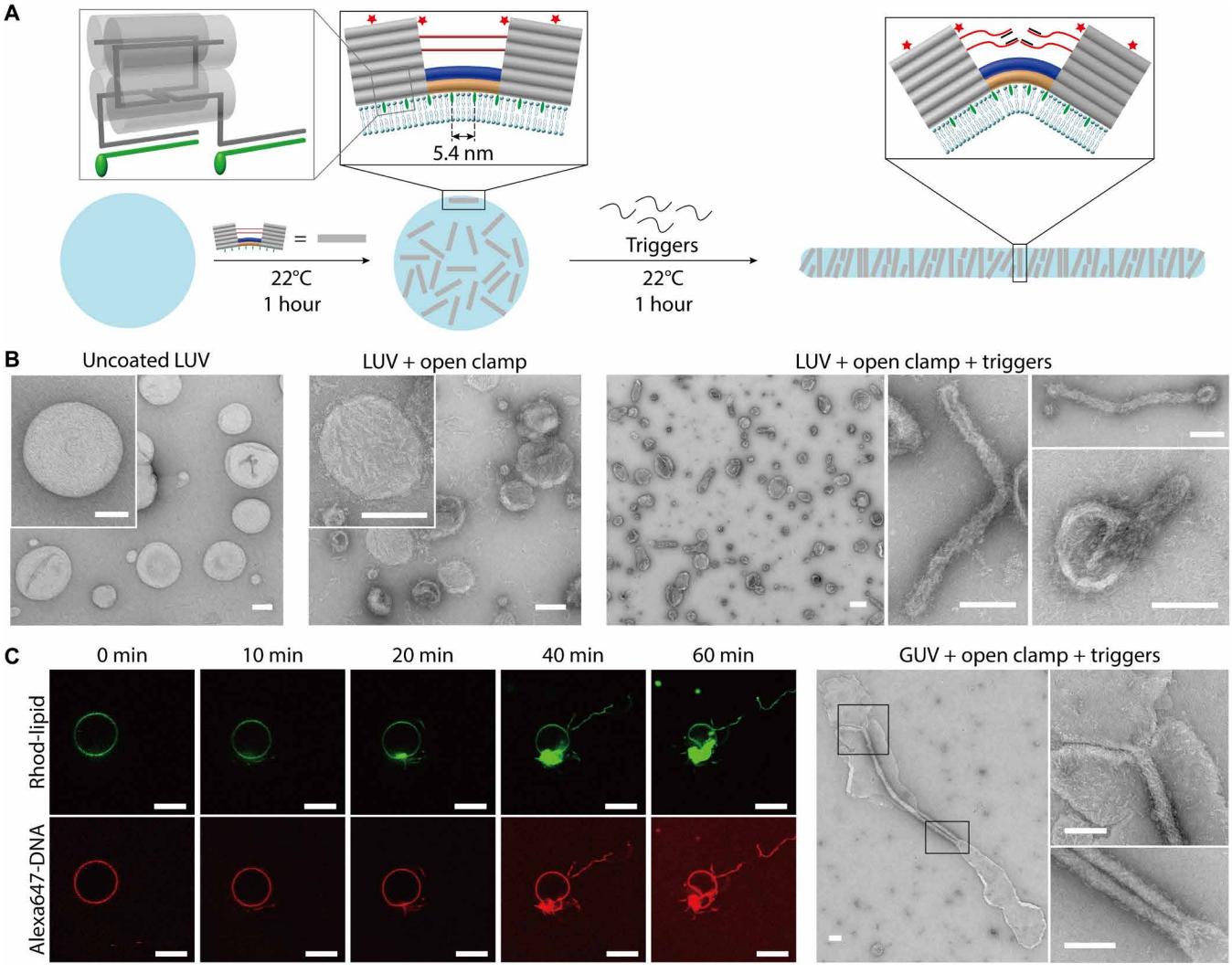

Fig. 2. Membrane tubulation driven by DNA clamp actuation. (**A**) A schematic of vesicle tubulation by actuating membrane-bound DNA clamps. Cholesterol and Alexa Fluor 647 modifications are depicted as green ellipsoids and red stars, respectively. Only staple strands (dark gray lines) of DNA helices (semitransparent cylinders) are shown in the left cartoon model for clarity. (**B**) LUV tubulation: TEM images of clamp-free LUVs (left); LUVs coated with open, tension-loaded clamps (middle); and clamp-coated LUVs after triggered conformational change (right). Scale bars, 100 nm. This experiment was repeated three times (technical replicates) with similar results. (**C**) GUV tubulation: Time-course study of tubulation events by confocal fluorescence microscopy (left) and TEM images of tubulated GUVs (right). Scale bars, 100 nm for TEM images and 10 μm for fluorescence microscopy images. This experiment was repeated three times (technical replicates) with similar results.

membrane tubes appeared on only ~10.9% of the GUVs ($N = 55$). In other words, actuating membrane-bound open clamps was about 4× more likely to induce tubulation than directly treating membranes with closed clamps despite a similar measured surface density of DNA clamps on GUVs (Fig. 3, B and D). A similar trend was observed on LUVs (fig. S9), although the difference was only ~2-fold. A possible explanation is that the open conformation of tension-loaded clamps exposed all membrane anchors for near-maximal membrane accessibility, while the closed clamps may obscure cholesterols under the curved bridge, making them less likely to insert into the lipid bilayer. Tubulation thus occurs more readily on vesicles with higher leaflet asymmetry (i.e., more membrane anchors inserted), which promotes spontaneous membrane curvature, and better DNA-membrane contact, which favors curvature coupling between DNA clamp and bilayer. This effect was more prominent on GUVs than LUVs, probably because the near-zero membrane curvature of the former further discriminates against the closed clamps with higher curvature. To test this hypothesis, we built two variants of the inherently closed DNA clamps with only four cholesterol moieties per clamp, one with cholesterols attached toward the ends of the structure and the other near the center. Quantifying the Alexa Fluor 647–labeled DNA clamps on the GUV surface showed that the closed clamps labeled with four cholesterols near the ends covered GUVs with a surface density comparable to those with eight cholesterol labels, while the center-labeled variant had significantly lower density on GUVs (Fig. 3B). Therefore, it is entirely possible for a closed DNA clamp to bind stably with a GUV using only a subset of its membrane anchors, thus being unable to use the energy generated by membrane insertion of all eight cholesterols for tubulation. Our data are consistent with the notion that the

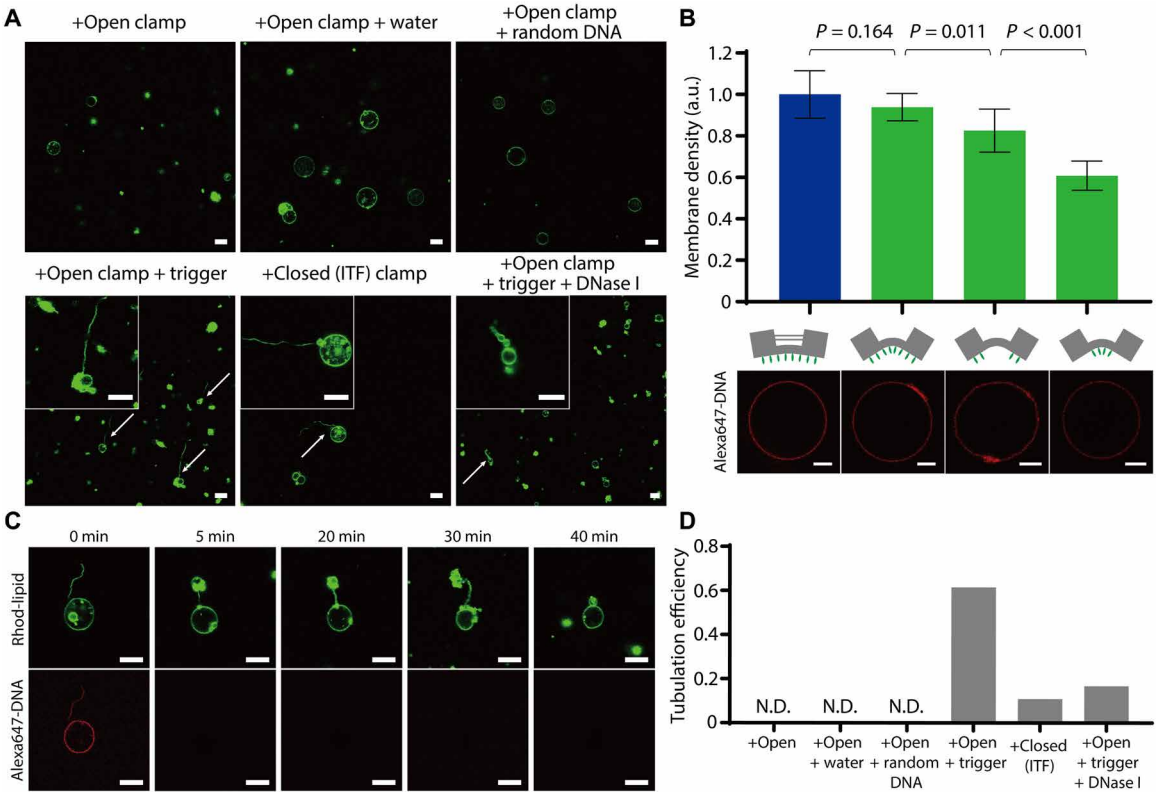

Fig. 3. Detailed study of GUV tubulation driven by DNA clamps. (**A**) GUVs after coincubation with DNA clamps. Reagents added to GUVs are noted on top of the corresponding fluorescence microscopy images. White arrows point to membrane tubes and tube-like structures. Scale bars, 10 μm. This experiment was repeated three times (technical replicates) with similar results. (**B**) Quantification of GUV surface coverage by open (blue bar) and closed (green bars) DNA clamps with various cholesterol modifications (schematics shown under the bar graphs). The membrane density of DNA clamps is calculated by dividing the integrated Alexa Fluor 647 (Alexa647) signal (pseudo-colored red in representative microscope images) by the vesicle's surface area within the confocal volume and normalized to the average density of the open clamp labeled with eight cholesterols. Bar graphs represent means ± SD, $N = 10$. P values are produced by unpaired two-tailed Student's t test (two-group comparison). Scale bars, 10 μm. a.u., arbitrary units. (**C**) Time-course study of a tubulated GUV after DNase I treatment (nuclease added at $t = 0$ min). Scale bars, 10 μm. This experiment was repeated three times (technical replicates) with similar results. (**D**) GUV tubulation efficiency (tubulated GUVs ÷ total GUVs) under various conditions, measured from fluorescence microscopy images such as those shown in (A). N.D., "not detected."

accessibility of membrane anchors is important for the membrane affinity of DNA nanostructures and that the energy revenue from membrane-anchor insertion must be sufficient to offset the energy expense of membrane remodeling for membrane-deforming DNA nanostructures (*9*, *32*). However, unlike the static DNA structures, reconfiguring tension-loaded DNA clamps released additional mechanical energy, presumably within a relatively short time window, which contributes toward membrane remodeling.

Removing DNA clamps from membrane tubes may lead to vesiculation

Membrane-tubulating proteins such as dynamin and ESCRT-III are thought to induce membrane scission and vesicle budding by depolymerization and membrane dissociation (*33*–*37*). It is thus interesting to ask whether removing DNA clamps from membranes can mediate the severing of membrane tubes or the formation of budding vesicles. We previously showed that membrane tubes originating from LUVs largely vanished after losing their DNA coat to enzymatic digestion (*10*). Here, we treated tubulated GUVs with deoxyribonuclease I (DNase I; an endonuclease that digests both ssDNA and double-stranded DNA) and monitored the membrane dynamics by confocal microscopy (Fig. 3C and fig. S10). Consistent with previous findings, most membrane tubes disappeared 1 hour after the addition of DNase I (tube-like structures remained on 16.7% of GUVs, $N = 42$), suggesting their reliance on DNA coats for stability. A time-course study revealed that tubular protrusions from GUVs already started to deform within 5 min of nuclease treatment, coincident with the disappearance of Alexa Fluor 647 signals from the GUV surface. At this stage, the membrane tube shortened while remaining connected to its parent GUV, with a second vesicle emerging at the distal end. This asymmetric dumbbell-like structure persisted for as long as 30 min, until the tube eventually disappeared, and the distal vesicle departed. In other incidents, the removal of DNA clamps appeared to cause the membrane tubes to break into multiple vesicles (Fig. 3A and fig. S10). It is notable that while most of the fluorescent labels and the cholesterol anchors were cut from the DNA clamps by DNase I within 5 min, some partially digested DNA structures existed for up to 40 min (fig. S11), which may linger and contribute to the tubular membranes that survived longer. Therefore, our data suggested a possible mechanism to artificially induce vesiculation by stripping narrow (tens of nanometers in width) membrane tubes of their stabilizing DNA coats.

Mechanics and shapes of DNA clamps modulate their membrane tubulation outcomes

Our working model is that the DNA clamps induce membrane tubulation by releasing the energy stored in the prestressed DNA bridge and imposing the curvature of the clamps on the membrane. Therefore, a reasonable hypothesis is that the eventual abundance and width of membrane tubes are tied to the amount of energy initially stored in the tension-loaded clamps. To systematically test this, we built a set of reconfigurable DNA clamps (named I, II, III, IV, and V) with nearly flat open conformations but with increasing curvatures in the closed conformations (fig. S12). All five clamps were designed using a common principle (minor changes are noted in the "Design considerations for highly curved DNA clamps" section in the Supplementary Materials). Therefore, those storing more energy in the tension-loaded (i.e., open) state should exhibit higher curvatures once the tension is released by triggered strand displacement. Assembling and actuating the DNA clamps in solution confirmed that all five versions of DNA clamps folded with a decent yield (fig. S13) and underwent structural transformation in response to the trigger strands (figs. S14 to S18). In general, most clamps adopted curvatures in good agreement with the design before and after reconfiguration, as measured from negative-stain TEM images (Fig. 4, A and B, and fig. S19). Notably, clamps IV and V, the two versions storing the most energy, folded with more defects (fig. S20) and greater deviation from expected curvatures (Fig. 4B and fig. S19) than the rest of the set. This is not surprising as DNA structures containing severely bent helices or highly tensioned ssDNA segments ($f > 20$ pN) are known to be prone to misfolding (*25*, *38*). Nevertheless, the clamps provided a toolset to investigate the correlation between the mechanical properties of DNA devices and their membrane-tubulating functions.

When deployed to GUVs, all five DNA clamps generated membrane tubes in a trigger-dependent manner (Fig. 4C and fig. S21). Actuating tension-loaded DNA clamps on membrane generally resulted in similar or higher tubulation efficiency compared with covering GUVs with inherently tension-free clamps. These behaviors are well represented by clamp II that we initially tested. Expectedly, clamps II and III drew much more (~6×) tubes from GUVs than clamp I, which probably does not release enough energy to nucleate the formation of a membrane tube. However, the tubulation efficiency did not increase further with the higher energy-storing capabilities of clamps IV and V, which showed considerably diminished membrane-remodeling activities. We attribute this to the relatively high occurrence of structural defects in these highly tensioned clamps (fig. S20). Such defective clamps can still bind to GUVs but may be unable to close and disperse energy properly, thus impeding the membrane tube elongation (figs. S22 and S23, table S3, and see the "Proposed mechanism of membrane tubulation" section in the Supplementary Materials for details) (*39*, *40*). Clamps IV and V tubulated LUVs as efficiently as clamps II and III (fig. S9), suggesting that some misfolded clamps may still participate in membrane remodeling, but their involvement makes it difficult to form membrane tubes of sufficient length to be detected by fluorescence microscopy.

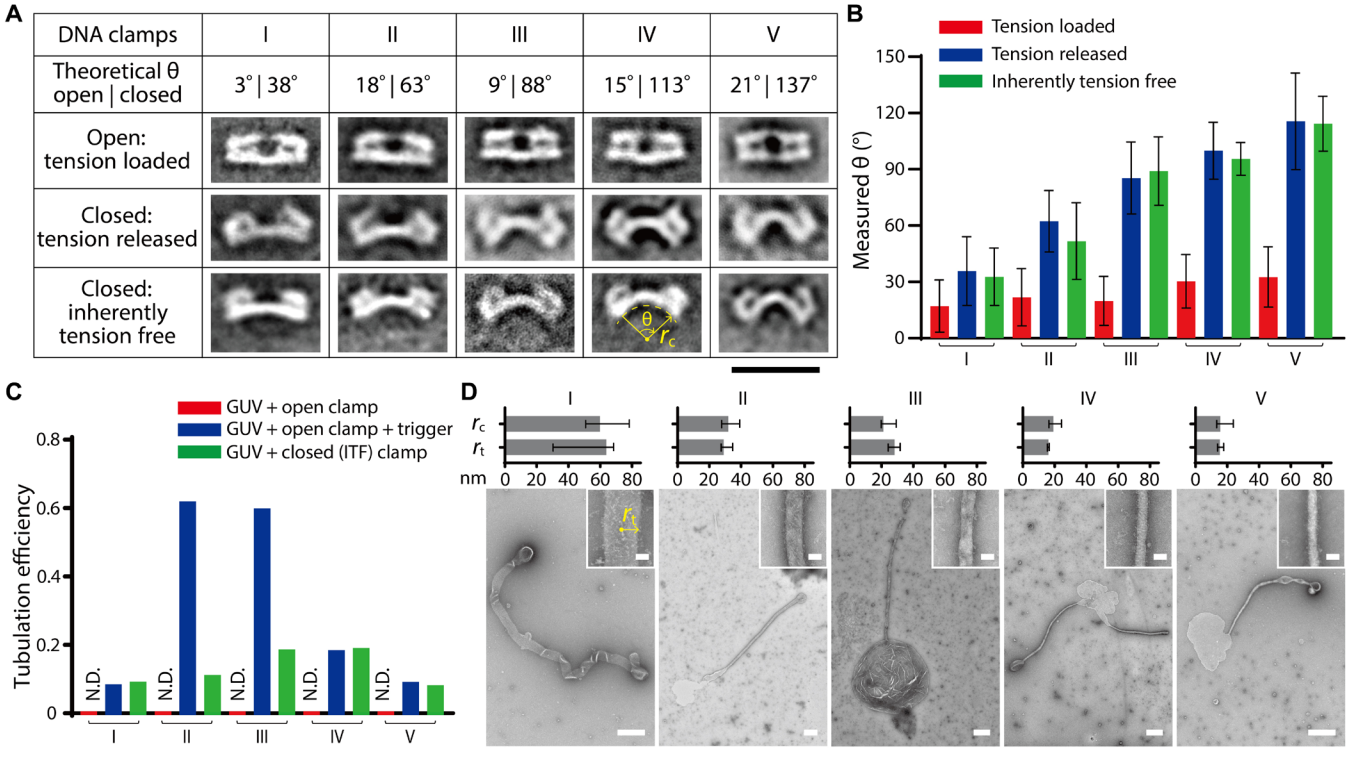

Fig. 4. GUV tubulation by DNA clamps with different curvatures. (**A**) Class-average TEM images of five different DNA clamps (named I to V with increasing curvatures) in open and closed conformations. Scale bar, 50 nm. (**B**) Bending angles (θ) measured from extender-attached DNA clamps. Bar graphs represent means ± SD. $N = 11$ to 28. (**C**) Efficiency of GUV tubulation induced by DNA clamps. $N = 33$ to 98. (**D**) Morphology of membrane tubules covered by DNA clamps with varying curvatures. Bar graphs (top) show the medians of r_c (radii of curvature of closed DNA clamps; $N = 11$ to 25) and r_t (radii of membrane tubes; $N = 11$ to 42) with 95% confidence intervals. TEM images (bottom) show representative tubulated GUVs. Scale bars, 400 nm. Insets show magnified regions of membrane tubes. Scale bars, 50 nm.

We next examined how the curvature of closed DNA clamps might influence that of the membrane tubes. For this, we calculated the radii of curvature (r_c) of the tension-released DNA clamps from their measured bending angles (figs. S19 and S24). The r_c value of each DNA clamp was then compared with the radius of membrane tubes (r_t) generated by actuating the clamp on GUVs (Fig. 4D). Notably, we found nearly identical r_c and r_t values for the entire set of clamps, strongly suggesting that the tension-release mechanism bent DNA clamps on GUVs as much as in solution and that the closed clamps wrapped the membranes tightly following the circumference of the tubes (fig. S24). However, this trend does not hold for LUVs (figs. S25 to S29 and table S2). Despite their very different shapes in the closed state (r_c value averaging 15 to 60 nm), all five DNA clamps gave rise to membrane tubes of similar widths (mean r_t = 15 to 20 nm). Thus, there seemed to be other determinants in addition to the geometry of DNA clamps that defined the width of membrane tubes. We suspect that the small size of extruded liposomes limited the lipid supply and led to a steep rise in membrane tension during membrane tubulation, making it difficult to form wide tubes of appreciable length (fig. S30 and see the "Proposed mechanism of membrane tubulation" section in the Supplementary Materials for details) (*39*, *40*).

DISCUSSION

DNA nanostructures with curved membrane-binding interfaces have shown their promise as programmable membrane-remodeling tools (*9*–*11*). However, to fully recapitulate the well-regulated subcellular membrane dynamics in an artificial system, there is a pressing need for signal-responsive nanodevices that manipulate membranes with predictable outcomes. The tension-loaded DNA clamps presented here stably bind to the membrane in an inactive form and transform into the remodeling-competent form only when DNA triggers release their internal tension, thereby providing a means to activate membrane-remodeling nanodevices with specific biochemical signals. Consistent with our design, we show that the DNA clamps tubulate GUVs most efficiently when the DNA structural transformation on the membrane releases energy sufficient for tube nucleation and elongation. The clamps were strong enough to deform GUVs under slightly hypoosmotic conditions. Moreover, the width of GUV-originated membrane tubes is dictated by the curvature of the DNA clamp's cholesterol-labeled surface, offering the opportunity to control membrane topography with rationally designed DNA nanostructures. We envision future development in the following areas. First, although our proof-of-concept study has shown that the design principle can be generalized to build dynamic DNA structures with various geometrical and mechanical properties, DNA clamps with high internal stress fold with suboptimal quality, which negatively affects their membrane tubulation efficiency. Alternative design and assembly methods that improve the integrity of the prestressed DNA nanostructures are thus desirable. Second, the DNA clamps are strong enough to deform synthetic vesicles ranging from several hundred nanometers to tens of micrometers in diameter. It would be interesting to see how these DNA devices perform on the plasma membrane of cells with complex chemical composition and underlying cytoskeleton. Third, with a rich library of nucleic acid chemistry and well-developed DNA-based logic gates (*41*–*49*), it should be possible to build membrane-deforming devices with sophisticated control mechanisms and diverse molecular triggers. Incorporating certain structure-switching motifs, such as those sensitive to light (*50*) or pH (*51*), into the DNA clamps might lead to faster DNA reconfiguration and membrane deformation. Last, the DNA clamp's ability to recognize and process DNA signals opens opportunities to recruit and coordinate nanodevices by messenger molecules, such that devices with different functions can work in concert to accomplish complicated tasks, such as sorting membrane-associated cargos, packaging them into vesicles, and delivering them to designated locations.

MATERIALS AND METHODS

Design and assembly of DNA origami structures

The DNA clamps and extenders were designed in caDNAno (figs. S1, S5, S12, and S13) (*52*). All DNA oligonucleotides were purchased from Integrated DNA Technologies. Unmodified staple strands (excluding the ssDNA strings) were purchased in a 96-well plate format with concentrations normalized to 100 μM. Oligonucleotides longer than 80 nt (ssDNA strings) were purchased in tube format and purified in-house by denaturing polyacrylamide gel electrophoresis. Oligonucleotides with fluorescent or cholesterol modifications (antihandles) were high-performance liquid chromatography–purified by the vender. Scaffold strands p1512 and p3024 were prepared using a previously reported method (*53*–*55*).

The open, tension-loaded clamps (Fig. 1A, left, and fig. S1) were assembled in two steps. For step 1: Mix p1512 scaffold strand (50 nM) and a pool of staple strands (300 nM each), excluding two staple strands in the bridge (inside the black box in fig. S1), in a TE buffer [5 mM tris-HCl and 1 mM EDTA (pH 8.0)] containing 12.5 mM $MgCl_2$, using a 36-hour thermal annealing protocol (80° to 65°C, −1°C/5 min; 64° to 24°C, −1°C/50 min; 12°C hold). For step 2: Add the two staples back into the solution above and anneal the batch using an 18-hour protocol (40° to 20°C, −0.1°C/5 min; 12°C hold). The two-step folding strategy is deemed to promote the folding of properly folded clamps, likely because incorporating ssDNA strings into the piers before forming the bridge reduces the clamp oligomerization mediated by ssDNA strings (figs. S3 and S4). To close the open DNA clamps, the four trigger strands were added to tension-loaded clamps (5 nM) in 40-fold molar excess and incubated for 1 hour at room temperature. Alternatively, water or DNA oligonucleotides with random sequences (table S4) were added in place of the trigger strands as a negative control.

The closed, inherently tension-free clamps (fig. S1) were assembled from p1512 scaffold strand (50 nM) and a pool of staple strands (300 nM each), excluding the four ssDNA strings, in a TE buffer containing 12.5 mM $MgCl_2$ using the 36-hour protocol. The two extenders (Fig. 1B and fig. S5) were assembled from p3024 scaffold strand (50 nM) and a pool of staple strands (300 nM) in a TE buffer containing 10 mM $MgCl_2$ using the 36-hour protocol.

All folded DNA origami structures—except the open, tension-loaded clamp V—were purified by PEG (polyethylene glycol) fractionation (*56*, *57*). Briefly, the assembled structures were supplemented with 8% (w/v) PEG-8000 and 0.5 M NaCl and held at room temperature for 10 min before centrifugation at 15,000*g* at 4°C for 15 min. The postcentrifugation supernatant was carefully removed by pipetting. The pellet was resuspended in a TE buffer containing 12.5 mM $MgCl_2$, followed by another round of PEG fractionation. The pellet was lastly dissolved in a TE buffer containing 12.5 mM $MgCl_2$ and stored at 4°C before usage.

The open, tension-loaded clamp V was purified by rate-zonal centrifugation (*58*). Typically, 0.5 ml of assembled product was concentrated to 0.2 ml using PEG fractionation, loaded on top of a 15 to 45% (v/v) quasi-linear glycerol gradient in a polycarbonate centrifuge tube (13 mm by 51 mm, Beckman Coulter Inc.), and spun at 50,000 rpm in a Beckman swing bucket rotor (SW55-Ti rotor) for 3 hours. The contents of the tube were fractionated from top to bottom (200 μl per fraction). Eight microliters of each fraction was then loaded onto a 1.5% agarose gel containing ethidium bromide (EtBr; 0.5 μg/ml) and run in 0.5× TBE (45 mM tris base, 45 mM boric acid, and 1 mM EDTA) and 10 mM $MgCl_2$ for 2 hours at 5 V/cm. After image analysis on a Typhoon FLA 9500 imager (GE Healthcare), the fractions containing well-formed monomeric DNA clamp were combined and concentrated using PEG fractionation. The pellet was then dissolved in a TE buffer containing 12.5 mM $MgCl_2$ and stored at 4°C before usage.

The concentrations of DNA origami structures were determined using a NanoDrop 2000 (Thermo Fisher Scientific). To attach DNA extenders to the clamp, a mixture of DNA clamp (5 nM), extenders (6 nM each), and linker strands (100 nM each) in a TE buffer containing 12.5 mM $MgCl_2$ was incubated at 30°C for 18 hours.

Preparation and tubulation of LUVs

LUVs composed of 99.2% DOPC and 0.8% Rhod-PE (lipids purchased from Avanti Polar Lipids) were produced by lipid-film rehydration and extrusion. Briefly, appropriate amounts of lipids in chloroform were mixed in glass tubes and dried in nitrogen gas for 30 min and under vacuum overnight. The lipid film was then suspended in 300 μl of hydration buffer [25 mM Hepes-KOH, 100 mM KCl, and 10 mM $MgCl_2$ (pH 7.4)] by agitation to achieve a final lipid concentration of 1 mM. The suspended lipids were frozen-thawed in plastic centrifuge tubes for seven cycles, each consisting of 15-s flash-freezing in liquid nitrogen followed by 2-min water bathing at 37°C. Final homogenization was achieved through 40 forward-and-back extrusion pumps using an Avanti mini-extruder with a 200-nm filter. The final LUVs were stored at 4°C for no more than 2 weeks before usage.

To bind DNA clamps to the surface of LUVs, Alexa Fluor 647–and cholesterol-labeled DNA clamps in hydration buffer were mixed with LUVs to achieve a final DNA clamp concentration of 25.5, 20.4, 10.2, or 0 nM (corresponding to a theoretical membrane coverage of 125, 100, 50, or 0%, respectively) and final lipid concentration of 20 μM. The mixtures were incubated for 1 hour. To actuate DNA clamps for membrane tubulation, 0.64 μl of trigger strands (25 μM each; dissolved in water) was added to 20 μl of DNA clamp–coated LUVs and incubated for another 1 hour. Alternatively, 0.64 μl of water was added in place of the trigger strands as a negative control. The entire procedure was carried out at room temperature.

Preparation of GUVs

GUVs composed of 99.2% DOPC and 0.8% Rhod-PE were produced by electroformation (*59*). Briefly, to form thin lipid films on indium tin oxide (ITO) glass slides, 125 μl of lipid solution (1 mg/ml) in chloroform was spotted on the conducting face of two glass slides within a marked 3 cm × 3 cm area; the chloroform was then evaporated on a 50°C heating plate. One piece of copper tape was placed on the conducting face of each slide, extending over the edge. Two of these ITO slides with lipid film–covered areas were aligned over each other, separated by a silicon slab containing a 3 cm by 3 cm by 3 mm ($L \times W \times H$) hole inside, to create a chamber accessible only via a syringe entry channel with copper tape extensions on opposite sides of the chamber. The sandwich was held together with binder clips, wrapped in foil, and placed in a vacuum chamber. After 1 hour, the chamber was filled with about 3 ml of sucrose solution containing 0.03% (w/v) sodium azide at an osmolarity of 207 mOsm (measured via a Thomas Scientific Micro-Osmette osmometer), which is 16 mOsm lower than the hydration buffer (223 mOsm) to prevent vesicle bursting. The filled chamber was sheltered from light with aluminum foil. The copper strips were connected to a waveform generator initially set at a frequency of 10 Hz, 0 phase, and 100-mVpp amplitude. The amplitude was gradually increased every 6 min as follows: 200 mV, 300 mV, 500 mV, 700 mV, 900 mV (each at 10 Hz), and then left at 1.2 V at 10 Hz for 1 hour, finishing with 1.4 V at 4 Hz for 30 min. The resulting GUVs were then carefully extracted using a 1.1-mm needle on a 2-ml syringe and stored in LoBind Eppendorf tubes at 4°C.

Negative-stain TEM

For DNA-only samples, a drop of the sample (5 μl) was deposited on a glow-discharged formvar/carbon-coated copper grid (Electron Microscopy Sciences), incubated for 1 min, and blotted away. The grid was first rinsed twice with 5 μl of TE buffer containing 12.5 mM $MgCl_2$, washed briefly with 5 μl of 2% (w/v) uranyl formate, and stained for 1 min with 5 μl of 2% uranyl formate. For samples containing liposomes, a drop of the sample (5 μl) was deposited on a glow-discharged formvar/carbon-coated copper grid, incubated for 4 min, and blotted away. The grid was then rinsed with 2% uranyl formate for 10 s and stained with 2% uranyl formate for 1 min. TEM images were acquired on a JEOL JEM-1400Plus microscope (acceleration voltage: 80 kV) with a bottom-mount 4 k × 3 k charge-coupled device camera (Advanced Microscopy Technologies). Negative-stain two-dimensional class averages were computed using EMAN2 (*60*).

Confocal fluorescence microscopy

A 10-μl drop of bovine serum albumin (BSA; 2 mg/ml) was placed on an uncoated MatTek glass-bottom dish, let sit for 20 min, and washed with hydration buffer. After that, a 10-μl drop of diluted GUV stock (~1.6× volume of hydration buffer added to 1 volume of stock) was dispensed on the BSA-coated region of the glass-bottom dish and let sit for 20 min to allow for GUV sedimentation on the glass surface. Subsequently, the unbound GUVs were removed by careful pipetting, immediately followed by the addition of 10 μl of hydration buffer (for imaging uncoated GUVs) or Alexa Fluor 647–and cholesterol-labeled DNA clamps (20.4 nM) in hydration buffer (for imaging DNA-coated GUVs). The mixtures were incubated for 1 hour. To actuate DNA clamps for membrane tubulation, 0.33 μl of trigger strands (25 μM each; dissolved in water) was added to clamp-coated GUVs and incubated for 1 hour. Alternatively, 0.33 μl of water or DNA oligonucleotides with random sequences (four oligos; 25 μM each; dissolved in water) were added as a negative control. To remove DNA coat from GUVs, 0.5 μl of DNase I stock solution (1 U/μl; Thermo Fisher Scientific) was added to tubulated GUVs and incubated for 1 hour. The GUVs were imaged under a Leica TCS SP8 confocal microscope using an HC PL APO CS2 63× oil objective lens. All experiments were conducted at room temperature. One milliliter of hydration buffer was spotted along the dish walls to mitigate evaporation. For transferring GUVs, micropipette tips (20 μl) were cut transversely to increase tip entry diameter and

reduce shear stress on GUVs. The clamp density (c) on the GUV surface was determined by the comparison between the Alexa Fluor 647 fluorescence density from the GUV surface and that in the bulk solution.

DNA-membrane affinity examined by density gradient centrifugation

Alexa Fluor 647– and cholesterol-modified DNA clamp (20.4 nM) were mixed with Rhod-labeled LUVs (20 μM lipid) in 60 μl of hydration buffer. This solution was incubated for 1 hour at room temperature for binding and then mixed with 120 μl of 45% iodixanol (STEMCELL Technologies) in hydration buffer. The 180 μl of solution (30% iodixanol) was added to the bottom of a 0.8-ml ultracentrifuge tube. Six additional 80-μl layers of iodixanol solution in hydration buffer (26, 22, 18, 14, 10, and 6% iodixanol per layer) were carefully stacked on top to form a final 6 to 30% iodixanol gradient. Gradients were spun at 48,000 rpm at 4°C in a SW55-Ti rotor for 5 hours. Fractions (42 μl each) were then collected from top to bottom of the gradient into a 96-well plate and imaged on a Typhoon FLA 9500 scanner for Alexa Fluor 647 and Rhod fluorescence, either directly or after agarose gel electrophoresis (see below).

Agarose gel electrophoresis

Samples and 1 kb of DNA ladder (New England Biolabs) were loaded into separate wells of a 1.5 or 2% agarose gel casted in running buffer (0.5× TBE and 10 mM $MgCl_2$) with EtBr (0.5 μg/ml) and run for 2 hours at 5 V/cm in running buffer. For lipid-containing samples, a final 0.05% SDS was added to the running buffer. The gel was scanned on a Typhoon FLA 9500 scanner. To recover purified DNA structures, bands of interest were excised on an ultraviolet transilluminator (VWR International) using a razor blade and spun in Freeze 'N Squeeze DNA gel extraction spin columns (Bio-Rad Laboratories).

SUPPLEMENTARY MATERIALS

Supplementary material for this article is available at https://science.org/doi/10.1126/sciadv.add1830

View/request a protocol for this paper from *Bio-protocol*.

REFERENCES AND NOTES

1. H. T. McMahon, J. L. Gallop, Membrane curvature and mechanisms of dynamic cell membrane remodelling. *Nature* **438**, 590–596 (2005).
2. J. H. Hurley, P. I. Hanson, Membrane budding and scission by the ESCRT machinery: It's all in the neck. *Nat. Rev. Mol. Cell Biol.* **11**, 556–566 (2010).
3. A. Frost, V. M. Unger, P. De Camilli, The BAR domain superfamily: Membrane-molding macromolecules. *Cell* **137**, 191–196 (2009).
4. S. M. Ferguson, P. De Camilli, Dynamin, a membrane-remodelling GTPase. *Nat. Rev. Mol. Cell Biol.* **13**, 75–88 (2012).
5. Q. Shen, M. W. Grome, Y. Yang, C. Lin, Engineering lipid membranes with programmable DNA nanostructures. *Adv. Biosyst.* **4**, 1900215 (2020).
6. M. Langecker, V. Arnaut, J. List, F. C. Simmel, DNA nanostructures interacting with lipid bilayer membranes. *Acc. Chem. Res.* **47**, 1807–1815 (2014).
7. A. Czogalla, H. G. Franquelim, P. Schwille, DNA nanostructures on membranes as tools for synthetic biology. *Biophys. J.* **110**, 1698–1707 (2016).
8. J. K. D. Singh, E. Darley, P. Ridone, J. P. Gaston, A. Abbas, S. F. J. Wickham, M. A. B. Baker, Binding of DNA origami to lipids: Maximizing yield and switching via strand displacement. *Nucleic Acids Res.* **49**, 10835–10850 (2021).
9. H. G. Franquelim, A. Khmelinskaia, J.-P. Sobczak, H. Dietz, P. Schwille, Membrane sculpting by curved DNA origami scaffolds. *Nat. Commun.* **9**, 811 (2018).
10. M. W. Grome, Z. Zhang, F. Pincet, C. Lin, Vesicle tubulation with self-assembling DNA nanosprings. *Angew. Chem. Int. Ed.* **57**, 5330–5334 (2018).
11. M. W. Grome, Z. Zhang, C. Lin, Stiffness and membrane anchor density modulate DNA-nanospring-induced vesicle tubulation. *ACS Appl. Mater. Interfaces* **11**, 22987–22992 (2019).
12. O. Birkholz, J. R. Burns, C. P. Richter, O. E. Psathaki, S. Howorka, J. Piehler, Multi-functional DNA nanostructures that puncture and remodel lipid membranes into hybrid materials. *Nat. Commun.* **9**, 1521 (2018).
13. K. Göpfrich, T. Zettl, A. E. C. Meijering, S. Hernández-Ainsa, S. Kocabey, T. Liedl, U. F. Keyser, DNA-tile structures induce ionic currents through lipid membranes. *Nano Lett.* **15**, 3134–3138 (2015).
14. H. G. Franquelim, H. Dietz, P. Schwille, Reversible membrane deformations by straight DNA origami filaments. *Soft Matter* **17**, 276–287 (2021).
15. C. M. A. Journot, V. Ramakrishna, M. I. Wallace, A. J. Turberfield, Modifying membrane morphology and interactions with dna origami clathrin-mimic networks. *ACS Nano* **13**, 9973–9979 (2019).
16. S. Dey, C. Fan, K. V. Gothelf, J. Li, C. Lin, L. Liu, N. Liu, M. A. D. Nijenhuis, B. Saccà, F. C. Simmel, H. Yan, P. Zhan, DNA origami. *Nat. Rev. Methods Primers* **1**, 13 (2021).
17. D. Y. Zhang, G. Seelig, Dynamic DNA nanotechnology using strand-displacement reactions. *Nat. Chem.* **3**, 103–113 (2011).
18. H. Ramezani, H. Dietz, Building machines with DNA molecules. *Nat. Rev. Genet.* **21**, 5–26 (2020).
19. M. DeLuca, Z. Shi, C. E. Castro, G. Arya, Dynamic DNA nanotechnology: Toward functional nanoscale devices. *Nanoscale Horizons* **5**, 182–201 (2020).
20. S. Nummelin, B. Shen, P. Piskunen, Q. Liu, M. A. Kostiainen, V. Linko, Robotic DNA nanostructures. *ACS Synth. Biol.* **9**, 1923–1940 (2020).
21. Q. Xiong, C. Xie, Z. Zhang, L. Liu, J. T. Powell, Q. Shen, C. Lin, DNA origami post-processing by CRISPR-Cas12a. *Angew. Chem. Int. Ed.* **59**, 3956–3960 (2020).
22. Y. Suzuki, I. Kawamata, K. Mizuno, S. Murata, Large deformation of a DNA-origami nanoarm induced by the cumulative actuation of tension-adjustable modules. *Angew. Chem. Int. Ed.* **59**, 6230–6234 (2020).
23. F. N. Gür, S. Kempter, F. Schueder, C. Sikeler, M. J. Urban, R. Jungmann, P. C. Nickels, T. Liedl, Double- to single-strand transition induces forces and motion in DNA origami nanostructures. *Adv. Mater.* **33**, 2101986 (2021).
24. Y. Ke, S. M. Douglas, M. Liu, J. Sharma, A. Cheng, A. Leung, Y. Liu, W. M. Shih, H. Yan, Multilayer DNA origami packed on a square lattice. *J. Am. Chem. Soc.* **131**, 15903–15908 (2009).
25. H. Dietz, M. D. Shawn, M. S. William, Folding DNA into twisted and curved nanoscale shapes. *Science* **325**, 725–730 (2009).
26. L. Zhou, A. E. Marras, H.-J. Su, C. E. Castro, DNA origami compliant nanostructures with tunable mechanical properties. *ACS Nano* **8**, 27–34 (2014).
27. T. Liedl, B. Högberg, J. Tytell, D. E. Ingber, W. M. Shih, Self-assembly of three-dimensional prestressed tensegrity structures from DNA. *Nat. Nanotechnol.* **5**, 520–524 (2010).
28. P. Virtanen, R. Gommers, T. E. Oliphant, M. Haberland, T. Reddy, D. Cournapeau, E. Burovski, P. Peterson, W. Weckesser, J. Bright, S. J. van der Walt, M. Brett, J. Wilson, K. J. Millman, N. Mayorov, A. R. J. Nelson, E. Jones, R. Kern, E. Larson, C. J. Carey, İ. Polat, Y. Feng, E. W. Moore, J. V. Plas, D. Laxalde, J. Perktold, R. Cimrman, I. Henriksen, E. A. Quintero, C. R. Harris, A. M. Archibald, A. H. Ribeiro, F. Pedregosa, P. van Mulbregt; SciPy 1.0 Contributors, SciPy 1.0: Fundamental algorithms for scientific computing in Python. *Nat. Methods* **17**, 261–272 (2020).
29. T. Zhang, C. Hartl, K. Frank, A. Heuer-Jungemann, S. Fischer, P. C. Nickels, B. Nickel, T. Liedl, 3D DNA origami crystals. *Adv. Mater.* **30**, 1800273 (2018).
30. K. N. Baumann, T. Schröder, P. S. Ciryam, D. Morzy, P. Tinnefeld, T. P. J. Knowles, S. Hernández-Ainsa, DNA–liposome hybrid carriers for triggered cargo release. *ACS Appl. Bio Mater.* **5**, 3713–3721 (2022).
31. N. De Franceschi, W. Pezeshkian, A. Fragasso, B. M. H. Bruininks, S. Tsai, S. J. Marrink, C. Dekker, A synthetic membrane shaper for controlled liposome deformation. *bioRxiv*, 2021.12.22.473854 (2021).
32. A. Khmelinskaia, H. G. Franquelim, E. P. Petrov, P. Schwille, Effect of anchor positioning on binding and diffusion of elongated 3D DNA nanostructures on lipid membranes. *J. Phys. D Appl. Phys.* **49**, 194001 (2016).
33. B. Marks, M. H. B. Stowell, Y. Vallis, I. G. Mills, A. Gibson, C. R. Hopkins, H. T. McMahon, GTPase activity of dynamin and resulting conformation change are essential for endocytosis. *Nature* **410**, 231–235 (2001).
34. S. M. Sweitzer, J. E. Hinshaw, Dynamin undergoes a GTP-dependent conformational change causing vesiculation. *Cell* **93**, 1021–1029 (1998).
35. P. V. Bashkirov, S. A. Akimov, A. I. Evseev, S. L. Schmid, J. Zimmerberg, V. A. Frolov, GTPase cycle of dynamin is coupled to membrane squeeze and release, leading to spontaneous fission. *Cell* **135**, 1276–1286 (2008).
36. T. J. Pucadyil, S. L. Schmid, Real-time visualization of dynamin-catalyzed membrane fission and vesicle release. *Cell* **135**, 1263–1275 (2008).
37. J. Schöneberg, M. R. Pavlin, S. Yan, M. Righini, I. H. Lee, L. A. Carlson, A. H. Bahrami, D. H. Goldman, X. Ren, G. Hummer, C. Bustamante, J. H. Hurley, ATP-dependent force generation and membrane scission by ESCRT-III and Vps4. *Science* **362**, 1423–1428 (2018).
38. P. C. Nickels, B. Wünsch, P. Holzmeister, W. Bae, L. M. Kneer, D. Grohmann, P. Tinnefeld, T. Liedl, Molecular force spectroscopy with a DNA origami–based nanoscopic force clamp. *Science* **354**, 305–307 (2016).

39. I. Derényi, F. Jülicher, J. Prost, Formation and interaction of membrane tubes. *Phys. Rev. Lett.* **88**, 238101 (2002).
40. A. Kessel, N. Ben-Tal, S. May, Interactions of cholesterol with lipid bilayers: The preferred configuration and fluctuations. *Biophys. J.* **81**, 643–658 (2001).
41. E. S. Andersen, M. Dong, M. M. Nielsen, K. Jahn, R. Subramani, W. Mamdouh, M. M. Golas, B. Sander, H. Stark, C. L. P. Oliveira, J. S. Pedersen, V. Birkedal, F. Besenbacher, K. V. Gothelf, J. Kjems, Self-assembly of a nanoscale DNA box with a controllable lid. *Nature* **459**, 73–76 (2009).
42. M. D. Shawn, I. Bachelet, M. C. George, A logic-gated nanorobot for targeted transport of molecular payloads. *Science* **335**, 831–834 (2012).
43. T. Gerling, F. W. Klaus, M. N. Andrea, H. Dietz, Dynamic DNA devices and assemblies formed by shape-complementary, non–base pairing 3D components. *Science* **347**, 1446–1452 (2015).
44. A. Kuzyk, Y. Yang, X. Duan, S. Stoll, A. O. Govorov, H. Sugiyama, M. Endo, N. Liu, A light-driven three-dimensional plasmonic nanosystem that translates molecular motion into reversible chiroptical function. *Nat. Commun.* **7**, 10591 (2016).
45. J. Song, Z. Li, P. Wang, T. Meyer, C. Mao, Y. Ke, Reconfiguration of DNA molecular arrays driven by information relay. *Science* **357**, eaan3377 (2017).
46. S. Li, Q. Jiang, S. Liu, Y. Zhang, Y. Tian, C. Song, J. Wang, Y. Zou, G. J. Anderson, J. Y. Han, Y. Chang, Y. Liu, C. Zhang, L. Chen, G. Zhou, G. Nie, H. Yan, B. Ding, Y. Zhao, A DNA nanorobot functions as a cancer therapeutic in response to a molecular trigger in vivo. *Nat. Biotechnol.* **36**, 258–264 (2018).
47. H. Ijäs, I. Hakaste, B. Shen, M. A. Kostiainen, V. Linko, Reconfigurable DNA origami nanocapsule for pH-controlled encapsulation and display of cargo. *ACS Nano* **13**, 5959–5967 (2019).
48. J. Wang, Z. Zhou, Z. Li, I. Willner, Programmed catalysis within stimuli-responsive mechanically unlocked nanocavities in DNA origami tiles. *Chem. Sci.* **12**, 341–351 (2021).
49. W. Engelen, C. Sigl, K. Kadletz, E. M. Willner, H. Dietz, Antigen-triggered logic-gating of DNA nanodevices. *J. Am. Chem. Soc.* **143**, 21630–21636 (2021).
50. H. Asanuma, T. Takarada, T. Yoshida, D. Tamaru, X. Liang, M. Komiyama, Enantioselective incorporation of azobenzenes into oligodeoxyribonucleotide for effective photoregulation of duplex formation. *Angew. Chem. Int. Ed.* **40**, 2671–2673 (2001).
51. J.-L. Mergny, L. Lacroix, X. Han, J.-L. Leroy, C. Helene, Intramolecular folding of pyrimidine oligodeoxynucleotides into an i-DNA motif. *J. Am. Chem. Soc.* **117**, 8887–8898 (1995).
52. S. M. Douglas, A. H. Marblestone, S. Teerapittayanon, A. Vazquez, G. M. Church, W. M. Shih, Rapid prototyping of 3D DNA-origami shapes with caDNAno. *Nucleic Acids Res.* **37**, 5001–5006 (2009).
53. P. M. Nafisi, T. Aksel, S. M. Douglas, Construction of a novel phagemid to produce custom DNA origami scaffolds. *Synth. Biol.* **3**, ysy015 (2018).
54. F. Praetorius, B. Kick, K. L. Behler, M. N. Honemann, D. Weuster-Botz, H. Dietz, Biotechnological mass production of DNA origami. *Nature* **552**, 84–87 (2017).
55. J. Sambrook, D. W. Russell, *Molecular Cloning: A Laboratory Manual, Chapter 3* (Cold Spring Harbor Laboratory Press, ed 3., 2001).
56. S. M. Douglas, J. J. Chou, W. M. Shih, DNA-nanotube-induced alignment of membrane proteins for NMR structure determination. *Proc. Natl. Acad. Sci. U.S.A.* **104**, 6644–6648 (2007).
57. E. Stahl, T. G. Martin, F. Praetorius, H. Dietz, Facile and scalable preparation of pure and dense DNA origami solutions. *Angew. Chem. Int. Ed.* **53**, 12735–12740 (2014).
58. C. Lin, S. D. Perrault, M. Kwak, F. Graf, W. M. Shih, Purification of DNA-origami nanostructures by rate-zonal centrifugation. *Nucleic Acids Res.* **41**, e40 (2013).
59. M. I. Angelova, S. Soléau, P. Méléard, F. Faucon, P. Bothorel, in *Trends in Colloid and Interface Science VI*, C. Helm, M. Lösche, H. Möhwald, Eds. (Steinkopff, 1992), pp. 127–131.
60. G. Tang, L. Peng, P. R. Baldwin, D. S. Mann, W. Jiang, I. Rees, S. J. Ludtke, EMAN2: An extensible image processing suite for electron microscopy. *J. Struct. Biol.* **157**, 38–46 (2007).

Acknowledgments: We thank the Yale West Campus Imaging Core for the assistance with fluorescence microscopy. **Funding:** This work is supported by NIH grants GM132114 and GM141669 and a Yale University faculty startup fund to C.L., an Agency for Science, Technology and Research Graduate Scholarship (Singapore) to Q.X., and a China Scholarship Council fellowship to C.X. **Author contributions:** L.L. initiated the project, designed and performed most of the experiments, analyzed the data, and prepared the manuscript. Q.X. assisted with vesicle preparation. C.X. prepared p1512 scaffold strand for folding DNA clamps. F.P. interpreted the data, proposed the mechanism of tubulation, and prepared the manuscript. C.L. initiated the project, designed and supervised the study, interpreted the data, and prepared the manuscript. All authors reviewed and approved the manuscript. **Competing interests:** The authors declare that they have no competing interests. **Data and materials availability:** All data needed to evaluate the conclusions in the paper are present in the paper and/or the Supplementary Materials.

Submitted 25 May 2022
Accepted 24 August 2022
Published 12 October 2022
10.1126/sciadv.add1830